Applied Physics A (2026) 132:167
https://doi.org/10.1007/s00339-026-09354-z

**Applied Physics A**
**Materials Science & Processing**

# Near-Infrared light detection properties of n-$WS_2$/AlN/p-Si SIS heterostructures

**Meltem Donmez Kaya**[1,2]

Received: 23 October 2025 / Accepted: 17 January 2026
© The Author(s) 2026

**Abstract**

In this study, n-$WS_2$/AlN/p-Si semiconductor-insulator-semiconductor (SIS) heterostructures were fabricated using the RF magnetron sputtering technique with varying $WS_2$ deposition times. The structural and morphological properties of the produced heterostructures were characterized using XRD, SEM, and AFM measurements. While the formation of the $WS_2$ phase with a hexagonal structure was confirmed by XRD results, it was determined from SEM and AFM analyses that the crystallinity improved but the surface roughness increased with increasing the thickness of the $WS_2$ thin film. The optical properties of the heterostructures were further examined by UV–Vis–NIR spectroscopy and photoluminescence (PL) measurements, providing insight into thickness-dependent absorption behavior and defect-related optical transitions. Furthermore, the effect of the $WS_2$ layer thickness on the photoresponse characteristics of the fabricated heterostructure was systematically investigated. Considering the photoresponsiveness characteristics investigated with current-voltage measurements in the dark and under 780 nm illumination, the device, fabricated with a $WS_2$ thin layer of approximately 10 nm thickness, demonstrates high performance with a photoresponsiveness of 1.058 A/W at low voltage. These findings show that $WS_2$/AlN/Si SIS heterojunctions, which possess an excellent carrier transport mechanism, indicate strong potential for next-generation high-performance optoelectronic applications.

**Keywords** $WS_2$ · AlN · Heterojunction · Responsivity · Photodetector · Magnetron sputtering

## 1 Introduction

Photodetectors are devices that have important applications in various fields such as environmental monitoring, optical communication and imaging, and studies on the development of these devices continue intensively [1–3]. In general, photodetectors can operate in two different modes: photoconductive and photovoltaic. Photoconductive photodetectors require an external power source to separate charge carriers. This makes it difficult to produce devices in smaller sizes and lighter weight. However, self-powered photodetectors operating in photovoltaic mode generate a sufficient potential to effectively separate charge carriers and can therefore be produced in smaller sizes. Thanks to these features, it has become an interesting research area recently, offering many advantages. In this context, interest in photodetectors produced with two-dimensional materials has increased significantly in order to improve the properties such as sensitivity, response time and detection ability that determine the performance of photodetectors [4]. Tungsten disulfide ($WS_2$), an important member of the transition metal dichalcogenides family among two-dimensional materials, attracts great attention from researchers due to its layered structure and extraordinary electro-optic properties [5–7]. The electro-optic properties of $WS_2$, which has a tunable band gap ranging from 1.4 to 2.1 eV, vary significantly with thickness [8]. Various methods such as physical vapor deposition, chemical vapor deposition and sol-gel have been used for the growth of $WS_2$ [9–11]. The RF magnetron sputtering technique, which is among the physical vapor deposition methods, enables the production of large-area and cost-effective thin films thanks to the control of growth parameters such as deposition time, temperature and pressure [12].

✉ Meltem Donmez Kaya
meltmdn@gmail.com; meltemdonmez@gazi.edu.tr

[1] Gazi University, Photonics Application and Research Center, Ankara 06500, Turkey

[2] Department of Photonics, Gazi University, Ankara 06500, Turkey

Published online: 12 February 2026

Recently, extensive research has been conducted on heterojunction devices formed by the integration of two-dimensional (2D) materials onto Silicon (Si) [13–16]. Significant progress has been made on the development of heterojunction-based photodetectors, especially $WS_2$/Si and $MoS_2$/Si [17–20]. However, studies on the formation of semiconductor-insulator-semiconductor (SIS) heterojunctions, which offer an important avenue for improving the properties of photodetectors, are still limited. Although studies on photodetectors based on $WS_2$/Si have become quite popular recently, the effect of an insulating interlayer in these heterostructures has not been investigated sufficiently and there is a significant gap in the literature on this subject. Since Si and $WS_2$ materials have different carrier polarities, adding an insulating layer with high dielectric constant, such as aluminum nitride (AlN), between these two materials is an effective method to create heterostructures with strong photovoltaic effects [21, 22]. An ultra-thin AlN film has been frequently preferred as an insulating layer in photodetectors developed with SIS heterostructures due to its properties such as wide band gap of approximately 6.20 eV, negligible electron affinity and high internal resistance, and the fact that these properties significantly reduce the self-heating level of the devices [23]. In previous studies, promising results have been reported for photodetector applications where SIS heterostructure were developed using 2D material and AlN interlayer. For example, Singh and his colleagues measured a high responsivity of 9.93 A/W at a wavelength of 900 nm for the $MoS_2$/AlN/Si heterojunction-based photodetector produced using the Pulsed Laser Deposition (PLD) method, and reported rise and fall times of 12.5 µs and 14.9 µs, respectively [24]. Using the sputtering technique, Kumar et al. fabricated $MoS_2$/Si and $MoS_2$/AlN/Si heterostructures, which demonstrated superior performance when employed in SIS heterojunction-based photodetectors. The fabricated devices exhibited responsivity values of 0.1245 A/W at 532 nm (Visible region) and 1.4743 A/W at 1064 nm (NIR region), along with rise and fall times of 3.32 µs and 4.73 µs, respectively [25]. These studies show that SIS heterostructure based on 2D material and fabricated using an AlN insulating interlayer has significant potential to improve photodetector performance.

**Table 1** Deposition parameters of the films

| Parameters | Optimized value for AlN | Optimized value for $WS_2$ |
|---|---|---|
| Working pressure | 3 mTorr | 10 mTorr |
| RF power | 75 W | 40 W |
| Substrate temperature | 450 ˚C | 450 ˚C |
| Deposition times | 3 min | 3 min, 14 min, 26 min |

In this study, the fabrication and characterization of SIS heterojunctions were carried out by placing an insulating AlN ultrathin film between the n-$WS_2$/p-Si heterostructure. Radio frequency (RF) magnetron sputtering technique, which provides controllable parameters and high coating quality, was used in the production process of all films. To the best of our knowledge, there is no study on photodetection based on $WS_2$/AlN/Si heterostructure fabricated by this technique. Therefore, the aim of this study is to provide information on the photodetection performances of our fabricated heterojunctions using light illumination at 780 nm wavelength.

## 2 Experimental

### 2.1 Fabrication of the $WS_2$/AlN/Si (SIS) heterostructure

$WS_2$ and AlN layers of the SIS heterostructure were produced using the RF magnetron sputtering system onto Si and CG substrates. Before the substrates were loaded into the system for thin film deposition, a thorough cleaning process was performed using deionized water and alcohol, followed by drying with nitrogen ($N_2$) gas. First, using an Al target with a diameter of 2 inches and 99% purity, the AlN thin film was deposited onto Si and CG substrates in an Ar: $N_2$ environment with a ratio of 8:2. After successfully depositing the AlN film, $WS_2$ thin films of varying thicknesses were deposited onto AlN-coated substrates using a 5-inch $WS_2$ target with 99.99% purity to obtain SIS heterostructures. The deposition parameters of AlN and $WS_2$ films were presented in Table 1. Three samples prepared from $WS_2$ films deposited for 3 min, 14 min, and 26 min were referred to as S1, S2, and S3, respectively. After the successful production of the $WS_2$/AlN/Si (SIS) heterojunctions, the Au metal layer for the top contact was deposited by thermal evaporation using an Au target. The parameters used in this process were: room temperature (RT), 300 W power, $10^{-5}$ Torr pressure, and 15 min of sputtering time. The Au top contact was patterned using a mask during the process. The schematic diagram of the fabricated $WS_2$/AlN/Si heterojunction device is shown in Fig. 1.

### 2.2 Characterizations

The structural analysis was performed using X-ray diffraction (XRD) patterns obtained from an X-ray diffractometer (APD 2000 PRO) equipped with a CuKα1 X-ray source (λ = 1.54178 Å). The morphology and thickness of the samples were analyzed using a scanning electron microscope (Hitachi-SU 8220 FEG-SEM). The surface roughness and

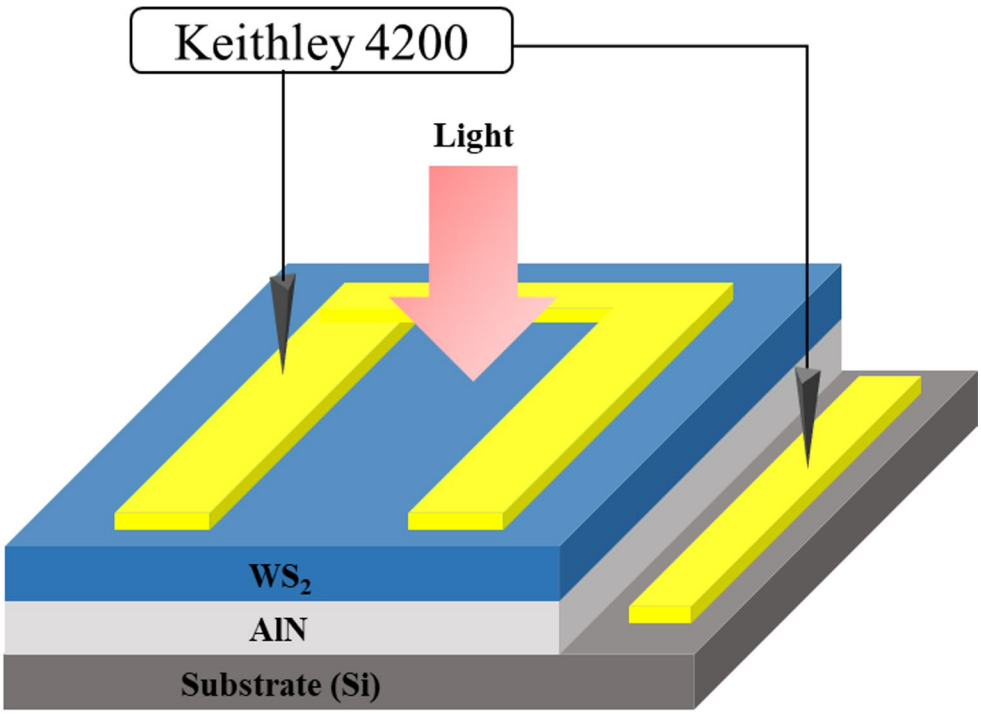



**Fig. 1** Schematic diagram of the measurement system and device

grain size were analyzed using an atomic force microscope (HP-AFM, NanoMagnetics Instruments Ltd., Oxford, UK). The optical properties were investigated using a UV–Vis-NIR spectrometer (PerkinElmer Lambda 2 S) in the wavelength range of 200–1100 nm. Photoluminescence (PL) measurements were carried out using a Jobin–Yvon Fluorolog-550 system under excitation by a 325 nm He–Cd laser. Furthermore, the electrical properties of the $WS_2$/AlN/Si heterojunction device were investigated through I–V measurements conducted with a Keithley 4200 semiconductor parameter analyzer system at room temperature.

## 3 Results and discussion

XRD analyses of $WS_2$/AlN/Si heterostructures with different $WS_2$ film thickness are presented in Fig. 2. Characteristic peaks belonging to the Si substrate and $WS_2$ are observed. Although no diffraction peaks of the ultrathin AlN interlayer are observed in the XRD pattern due to its ultra-thin nature, the presence of this interlayer contributes to improving the crystal quality by controlling the crystal orientation during the deposition of $WS_2$ films, as demonstrated in the work of Wang et al. [26]. All peaks observed for $WS_2$ in the XRD pattern are consistent with the Bragg reflections in JCPDS card number 08–0237, and the prominent peaks can be assigned to the (102) and (105) planes, corresponding to the hexagonal crystal structure for $WS_2$ [27]. In addition, the increase of the peak intensities with increasing film thickness can be attributed to $WS_2$ exhibiting a higher degree of crystallization [28]. The remaining peaks in the XRD patterns originate from the Si substrate [29].

The surface morphology and cross-sectional structure of the $WS_2$/AlN/Si thin films deposited with varying $WS_2$ deposition times are characterized by SEM, as shown in Fig. 3a and b, respectively. SEM surface images show that all samples have smooth and homogeneous surface morphologies. However, no $WS_2$ crystallization is observed in sample S1. Sample S2 exhibits a structure with a low degree of crystallization containing microcrystals. As the deposition time increased, the thickness increased, resulting in more pronounced crystallization in sample S3. Surface images of $WS_2$/AlN/Si heterojunctions produced with $WS_2$ films with different deposition times support the XRD findings regarding crystallization. Hotovy at al. produced four different samples by varying the W layer thickness between 1 nm and 28 nm to obtain $WS_2$ films via sulfurization. They reported that crystal quality improved with increasing thickness [30]. Correlating the images obtained from their SEM examinations with XRD results is consistent with the findings obtained in this study. The SEM surface morphology images of all investigated $WS_2$/AlN/Si heterojunction thin films described above differ from the findings reported in our previous study, which examined samples deposited without using substrate temperature [31]. The current samples were prepared at 450 °C substrate temperature, while previous experiments were conducted at room temperature. $WS_2$/AlN/Si films deposited at room temperature generally

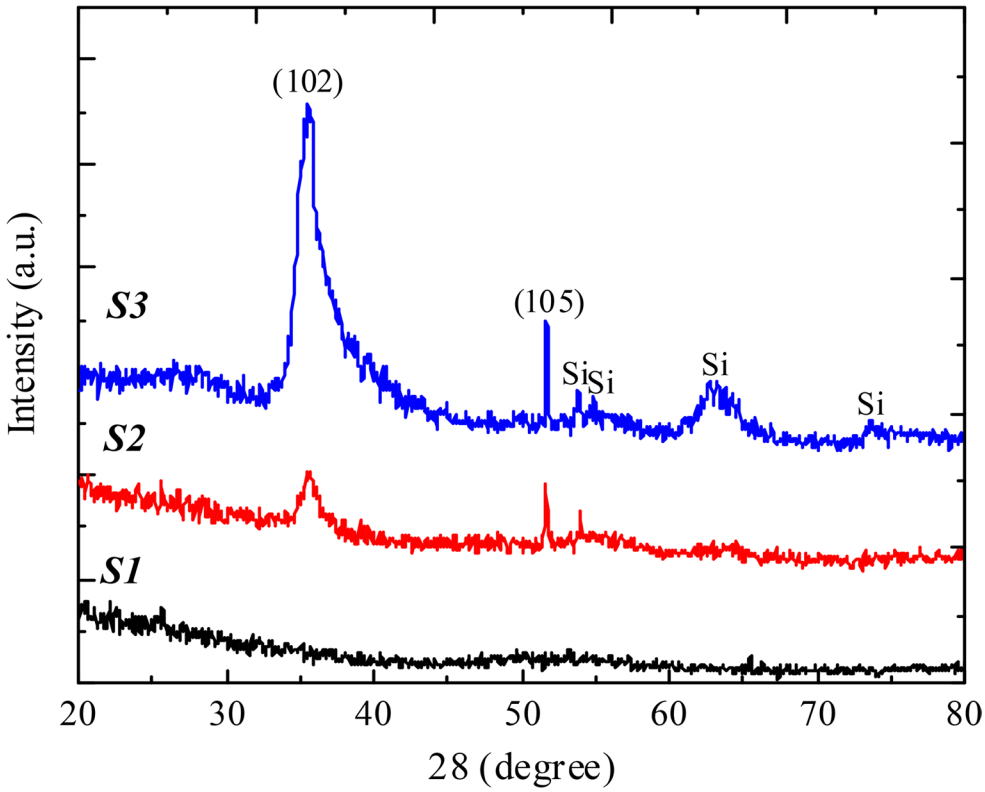



**Fig. 2** XRD patterns of samples deposited on a Si substrate

exhibited a rock-like microstructure containing $WS_2$ crystallites [32]. In contrast, samples obtained at 450 °C substrate temperature exhibited a rod-like microstructure [33].

Moreover, cross-sectional SEM images of all examined samples are used to determine the physical thicknesses of the $WS_2$ and AlN films. As seen from the SEM cross-sectional images in Fig. 3b, the thicknesses of $WS_2$ and AlN films are observed as $WS_2$: 11.4 nm, AlN: 10.9 nm; $WS_2$: 69.5 nm, AlN: 9.92 nm; and $WS_2$: 229 nm, AlN: 10.9 nm for samples S1, S2, and S3, respectively. Since thicknesses from SEM images are only approximately determined using scale bars, ± deviations may occur in the measured values [34].

Following SEM measurements of the samples, two and three-dimensional images of the surface morphologies and morphological parameters such as surface roughness and grain sizes were determined by AFM analysis. Figure 4 shows the surface morphologies of samples S1, S2, and S3 in two- and three-dimensional views obtained from a $3 \times 3$ $\mu m^2$ scan area.

AFM images reveal that as the $WS_2$ film thickness increases, the grain size increases, and the surface acquires a more homogeneous morphology. Parallel to this increase in film thickness, the surface roughness values were measured as 0.532 nm, 2.065 nm, and 2.147 nm, respectively, as presented in the Table 2. This increase indicates that the film thickness promotes nanostructure formation and leads to significant changes in surface topography. The AFM findings are consistent with the SEM analyses, with both techniques confirming the effect of increasing thickness on surface morphology. Increased surface roughness due to increased film thickness can lead to structural and electronic defects, negatively impacting photodetector performance [35, 36]. Therefore, it is of great importance to keep surface defects in electronic devices to the lowest possible level.

Optical transmittance and absorbance spectra of $WS_2$/AlN/Si films of different thicknesses are shown in Fig. 5a and b, respectively. As expected, samples prepared using thinner $WS_2$ films exhibit higher transmittance in the visible region, while transmittance decreases with increasing film thickness due to the increasing optical path length. In the ultraviolet and visible regions, strong absorbance is observed, attributed to band-to-band transitions in $WS_2$ [37]. In all samples, absorbance decreases significantly as the wavelength increases towards the near-infrared (NIR) region. However, the presence of a non-negligible level of absorbance at NIR wavelengths supports the ability of samples S1, S2, and S3 to interact with NIR region photons. This optical behavior confirms the suitability of the $WS_2$/AlN/Si heterojunction for NIR photodetection applications [38, 39]. Similarly, the literature reports that despite a decrease in absorbance in the NIR region in multilayer transition metal dichalcogenide (TMD) films, a significant level of absorption is observed, highlighting the usability

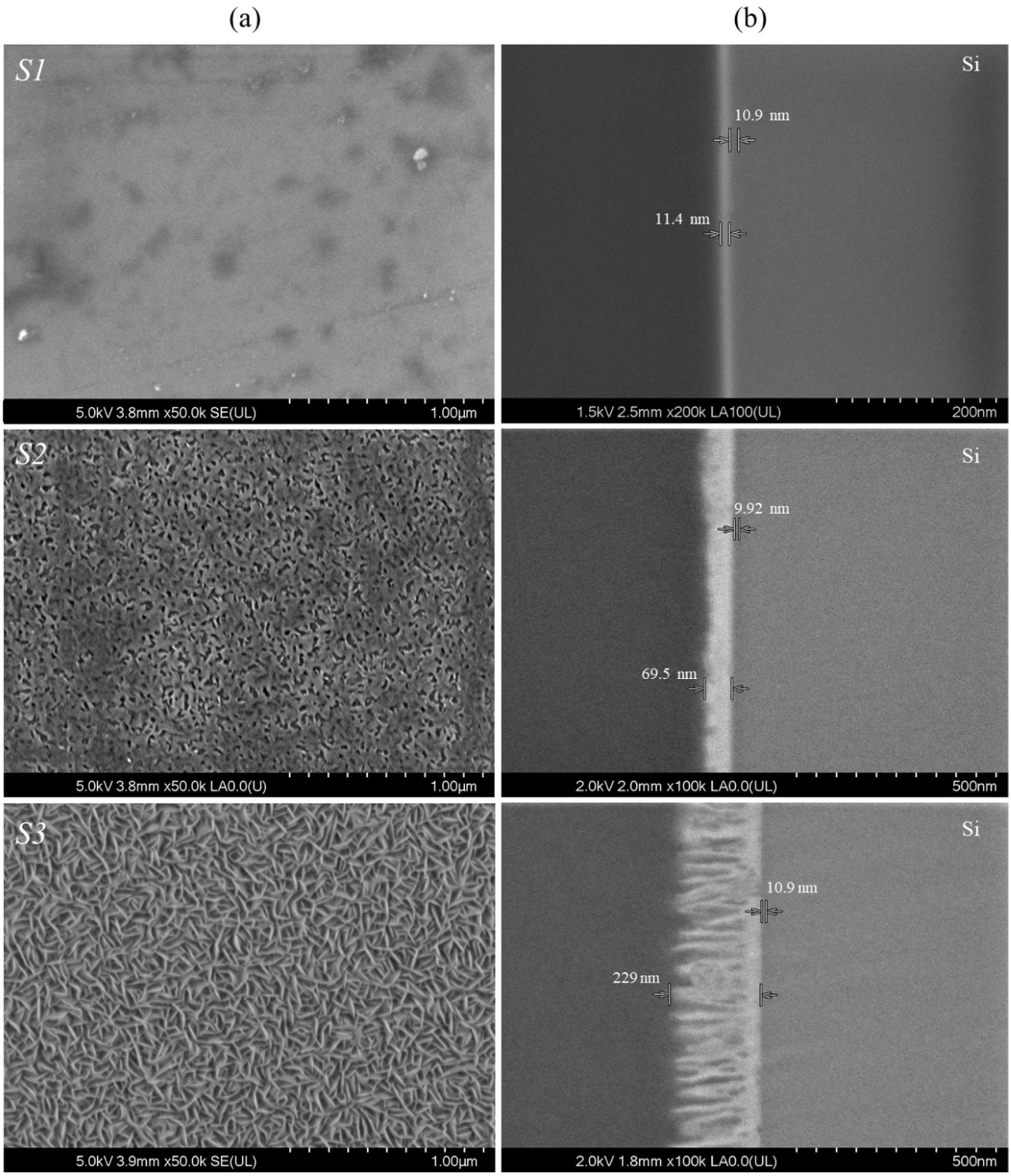



**Fig. 3** SEM images of the samples: **a** surface structure, **b** cross-sectional morphology

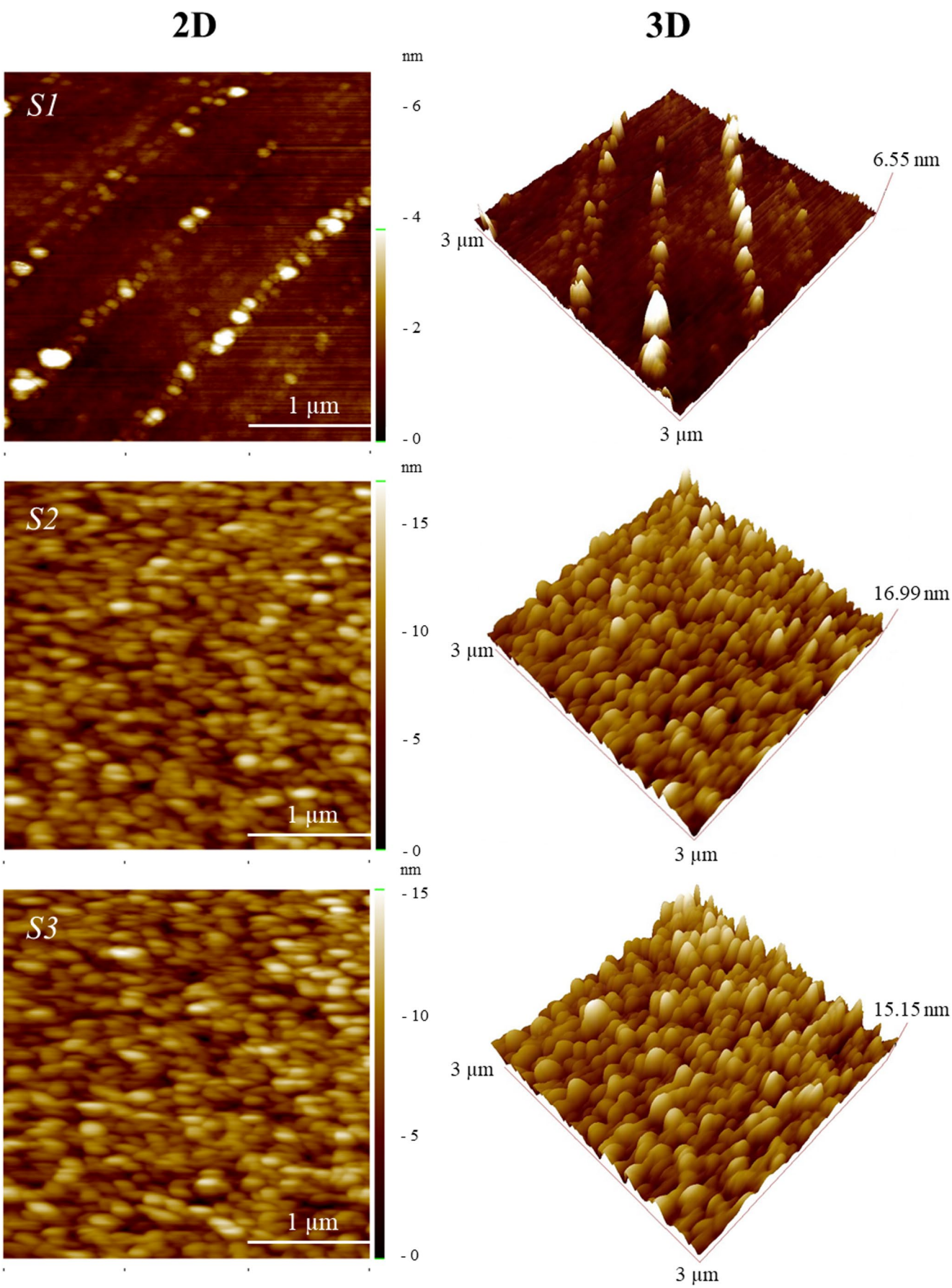

2D
3D
S1
nm
- 6
- 4
- 2
- 0
1 µm
6.55 nm
3 µm
3 µm
S2
nm
- 15
- 10
- 5
- 0
1 µm
16.99 nm
3 µm
3 µm
S3
nm
- 15
- 10
- 5
- 0
1 µm
15.15 nm
3 µm
3 µm

**Fig. 4** Two- and three-dimensional AFM scans of the S1, S2, and S3 samples

of these structures in NIR photodetection applications [40]. The optical band gap ($E_g$) was estimated using the Tauc relation, $(\alpha h\nu)^{1/\gamma} = \beta(h\nu - E_g)$, where hν represents the incident photon energy, α is the absorption coefficient, β is a proportionality constant, and γ denotes the nature of the optical transition. As shown in Fig. 5c, the extracted optical band gap values for the $WS_2$ films were determined to be 4.71 eV, 4.53 eV, and 3.53 eV for S1, S2, and S3, respectively, based on the indirect allowed transition. While these results suggest a stronger photodetection capability in the UV region, the presence of non-negligible absorption in the near-infrared (NIR) region indicates that the $WS_2$/AlN/Si heterostructure also possesses the potential for photodetection at NIR wavelengths.

Figure 6 shows the photoluminescence (PL) spectra of $WS_2$/AlN/Si heterojunctions formed using $WS_2$ at different film thicknesses (10, 50, and 100 nm). Photoluminescence (PL) spectra of the $WS_2$/AlN/Si heterostructures were recorded at room temperature using a 325 nm (3.82 eV) He–Cd laser excitation. The spectra exhibit a broad and multi-band emission profile, reflecting the defect-rich and polycrystalline nature of magnetron-sputtered films. Weak but discernible features observed around ~ 2.0 eV and ~ 2.4 eV are attributed to the A and B excitonic transitions of $WS_2$, arising from spin–orbit splitting of the valence band at the K point, although their significant broadening indicates enhanced disorder and exciton–defect interactions compared to exfoliated or CVD-grown layers [41–44]. The dominant emission band centered in the 2.7–3.1 eV range is assigned to defect-related radiative recombination in the AlN layer and/or at the $WS_2$/AlN interface, commonly associated with aluminum vacancies and oxygen-related complexes, which are efficiently activated under above-bandgap UV excitation [45, 46]. In addition, a low-energy emission component extending into the 1.6–1.8 eV region is observed, suggesting the presence of sub-bandgap localized states or defect-assisted recombination pathways in $WS_2$ and at the heterointerface. This sub-bandgap PL component is particularly relevant for near-infrared photodetection at 780 nm (1.59 eV), as it supports trap- or interface-mediated absorption and carrier generation beyond intrinsic band-edge transitions. Overall, the PL response indicates that optical activity in the $WS_2$/AlN heterostructures is governed by the combined contribution of $WS_2$ excitonic states and AlN/ interface defect levels, which, while broadening the emission spectrum, can facilitate NIR photoresponse through defect-assisted absorption and photogating mechanisms in $WS_2$-based photodetectors [47–49].

The PL response is strongly correlated with the optical absorption and structural characteristics revealed by UV–Vis–NIR spectroscopy and X-ray diffraction (XRD). Under 325 nm excitation, the monotonic increase in PL intensity from S1 to S3 follows the same trend observed in the UV absorbance (200–400 nm), indicating that enhanced photon absorption leads to a higher density of photo-generated carriers available for radiative recombination. XRD analysis further shows that the S3 sample exhibits a more pronounced diffraction peak, suggesting improved crystallinity and/or preferential orientation, which can reduce non-radiative recombination losses and contribute to the overall enhancement of PL intensity. However, the persistence of a dominant broad emission band in the 2.7–3.1 eV range confirms that defect-related states in the AlN layer and at the $WS_2$/AlN interface remain the primary radiative centers, even in the more structurally ordered films. Importantly, UV–Vis–NIR measurements reveal finite absorption in the near-infrared region, with the S2 sample exhibiting the highest absorbance around 780 nm (1.59 eV). Combined with the low-energy PL component observed at ~1.6–1.8 eV, this finding supports a defect- or interface-assisted sub-bandgap absorption mechanism enabling carrier generation at the target operating wavelength. Consequently, while S3 benefits from improved crystallinity and potentially superior carrier transport properties, S2 offers enhanced NIR photon harvesting, highlighting a trade-off between optical absorption and structural quality that is expected to directly impact the responsivity, speed, and stability of $WS_2$/AlN-based photodetectors operating at 780 nm.

I–V measurements performed under dark and illuminated conditions (780 nm) to evaluate the photodetector performance of three different $WS_2$/AlN/Si SIS heterojunctions, fabricated with varying $WS_2$ thicknesses, are presented in Fig. 7. The I–V characteristics of the fabricated $WS_2$/AlN/Si heterostructure devices (S1–S3) demonstrate the relationship between the applied bias and the resulting current. Measurements conducted under dark conditions and under 780 nm illumination reveal that all samples exhibit a pronounced increase in current compared to the dark state, both at zero bias and under applied bias. This increase clearly highlights the influence of the $WS_2$ layer thickness on the photoresponse of the SIS heterojunction devices. When examined especially in the zero-bias condition, it can be seen that the difference between the current values of the S1 sample in dark and illumination conditions is larger compared to the S2 and S3 samples.

The photocurrent can be calculated as $I_{ph} = I_{light} - I_{dark}$. Here, $I_{light}$ represents the current measured under light conditions, and $I_{dark}$ represents the current measured under dark conditions. The photoresponse properties of the fabricated devices were evaluated based on

**Table 2** Morphological parameters and optoelectronic performance values for the samples

| Sample Code | RMS (nm) | Grain Size (nm) | $I_{ph}$ (A) | $R$ (A/W) |
|---|---|---|---|---|
| S1 | 0.532 | 23.33 | 0.041 | 1.058 |
| S2 | 2.065 | 39.56 | 0.005 | 0.133 |
| S3 | 2.147 | 44.82 | 0.003 | 0.100 |

this formulation, and the corresponding photocurrent values are summarized in Table 2. Figure 8a and b present the variation of photocurrent and responsivity as a function of $WS_2$ film thickness, respectively.

The electrical photoresponse of the $WS_2$/AlN/Si heterostructures is consistently explained by the combined structural and optical characterization results shown in Figs. 1, 5 and 6, and 8. As shown in Fig. 8, the photocurrent–voltage (I–V) characteristics measured under 780 nm illumination exhibit a linear behavior, indicating predominantly ohmic and photoconductive transport. Notably, the highest photocurrent is obtained for the thinnest $WS_2$ layer (S1, 11.4 nm), while thicker films (S2, 69.5 nm; S3, 229 nm) show significantly reduced and nearly identical photocurrent levels. This behavior demonstrates that the photoresponse at 780 nm is not limited by optical absorption but rather by carrier transport and extraction efficiency. UV–Vis–NIR spectra (Fig. 5) reveal finite sub-bandgap absorption in the near-infrared region, confirming that carrier generation at 1.59 eV is possible; however, increased NIR absorbance in S2 and S3 does not translate into higher photocurrent, indicating inefficient carrier collection. The PL spectra recorded under 325 nm excitation (Fig. 6) show strong and broad defect-related

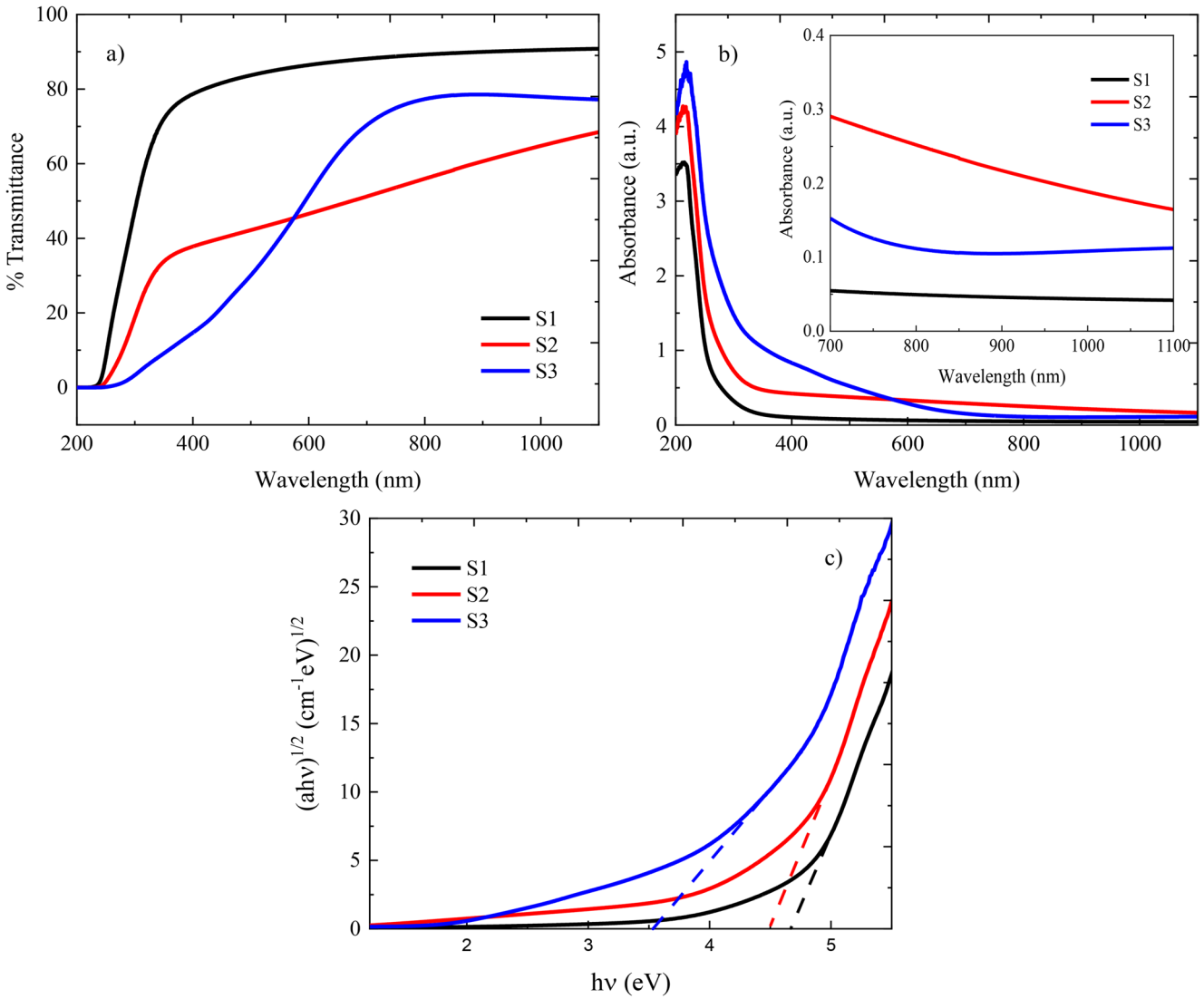



**Fig. 5** **a** Optical transmittance spectra of S1, S2, and S3 samples prepared using $WS_2$ films of different thicknesses, and (**b**) corresponding absorbance spectra. The inset shows the 700–1100 nm wavelength range, which is important for NIR photodetection. **c** Tauc plots showing the optical band gap energies

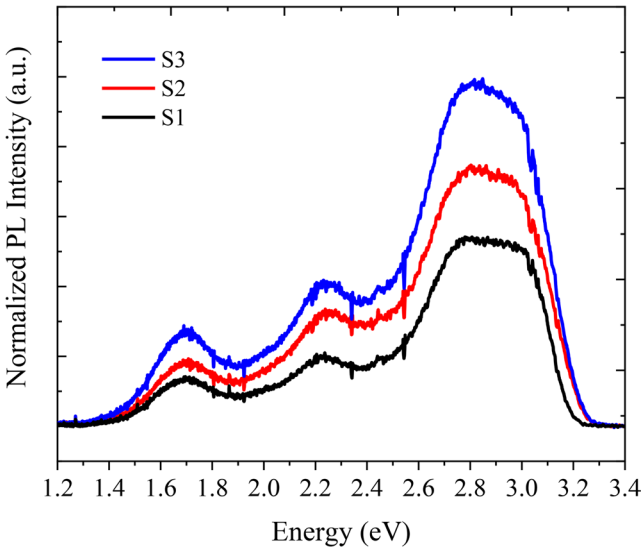



**Fig. 6** Photoluminescence characteristics of $WS_2$/AlN/Si heterostructures

emission bands, particularly in the 2.7–3.1 eV range, attributed to defect and interface states in the AlN layer and at the $WS_2$/AlN interface. Additionally, the presence of a low-energy PL component extending into the 1.6–1.8 eV region supports the existence of sub-bandgap localized states that enable NIR photoexcitation but simultaneously act as trapping and recombination centers, suppressing the net photocurrent in thicker $WS_2$ films. Although XRD analysis (Fig. 1) indicates improved structural ordering for S3, the absence of enhanced photocurrent suggests that crystallinity alone is insufficient to overcome trap-limited transport. Overall, the combined results indicate that the 780 nm photoresponse of the $WS_2$/AlN heterostructures operates in a transport-limited regime, where increased $WS_2$ thickness enhances defect-assisted absorption and radiative recombination but degrades carrier extraction, leading to optimal device performance in the thinnest $WS_2$ film. In addition, the fact that the photocurrent value of the developed NIR photodetector (S1) decreased by 1% after 20 cycles at 2-minute intervals under the same irradiation shows that the sensor is stable.

Responsivity is the photocurrent generated by the detector per unit optical power in response to light intensity when exposed to light of a specific wavelength [50–52]. The responsivity of the prepared devices was calculated using the following relationship:

$$R = I_{ph}/P_{in} \quad (1)$$

where $I_{ph}$ is the photocurrent and $P_{in}$ is the incident optical power on the detector. As can be seen from Fig. 8b, the responsivity shows a decreasing trend with increasing $WS_2$ film thickness. While sample S1 fabricated with a $WS_2$ film of approximately 10 nm thickness exhibited a high responsivity of 1.05 A/W, the responsivity of samples S2 and S3 decreased to 0.133 A/W and 0.100 A/W, respectively, as the layer thickness increased. The $WS_2$/AlN/Si heterojunction device with a responsivity of 1.058 A/W obtained in this study exhibits competitive performance compared to similar 2D material-based photodetectors reported in the literature. For example, in the work conducted by Yue et al., a $MoS_2$/Si heterojunction photodetector operating without an external bias was developed, and a responsivity of 0.047 A/W was reported in the NIR region [53]. In contrast, the $WS_2$/AlN/Si heterojunction device developed in this study achieved a high responsivity of 1.05 A/W in the NIR region. This finding demonstrates the strong capability of the proposed device to generate a high photo-response with low energy consumption. In another study, an Au/$WS_2$/$SiO_2$/Si-based photodetector was developed by Shahbazi and colleagues, and a responsivity of approximately 0.07 A/W was achieved at a wavelength of 635 nm under a 5 V bias [54]. In summary, compared to similar studies in the literature, the $WS_2$/AlN/Si-based photodetector developed in this study demonstrated strong performance thanks to its high responsivity at a wavelength of 780 nm.

Many studies have reported that placing an insulating layer of appropriate thickness, such as AlN, $Al_2O_3$, and $SiO_2$, at the heterojunction interface is significant for device performance [55, 56]. The insulating layer plays a critical role in determining the charge-carrying behavior and current-transfer mechanisms in heterojunction structures. AlN is a more advantageous insulating material compared to traditional insulators like $Al_2O_3$ and $SiO_2$ due to its wide band gap, high internal resistance, and low interface trap density. For instance, Yin et al. comparatively investigated the commonly used AlN, $Al_2O_3$, and $SiO_2$ insulating layers in the photodetector structures they developed and reported that the most successful device performance was obtained in structures using the AlN insulating layer [57]. To better understand the charge transport mechanism in the I–V characteristics, Fig. 9 shows the energy band diagram of the $WS_2$/AlN/Si SIS heterojunction and the carrier transport mechanism under forward bias. The bandgaps of $WS_2$, AlN, and Si reported in the literature are 1.4 eV, 6.2 eV, and 1.1 eV, respectively [58–60]. Furthermore, the electron affinities of these materials are reported to be approximately 4.2 eV, < 2 eV, and 4.05 eV, respectively [61, 63]. In the forward bias case, as the bias voltage increases, carriers gradually begin to accumulate at the $WS_2$/AlN interface. This accumulation process continues until the system reaches a certain threshold voltage. Once this threshold is exceeded, the accumulated charge carriers rapidly tunnel through the AlN insulator layer, generating a sudden and significant current increase. Because carrier transfer in SIS heterojunctions

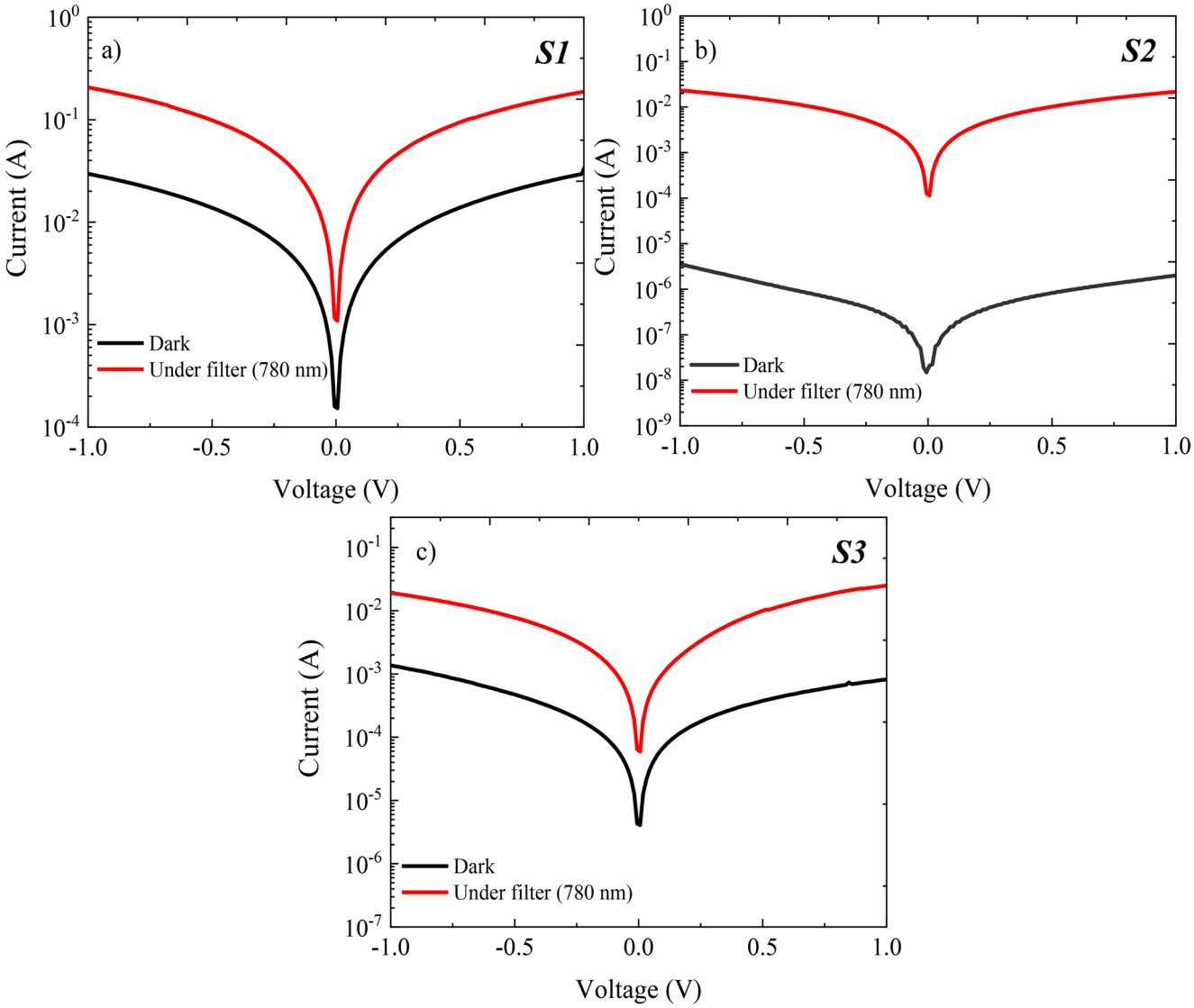



**Fig. 7** I–V characteristics of the obtained devices in dark and light conditions: **a** sample S1, **b** sample S2, **c** sample S3

occurs through tunneling, these structures exhibit much higher current flow than p–n heterojunctions. Thus, SIS heterojunctions exhibit high conductivity even at low forward voltages, which is a significant advantage for high-performance optoelectronic applications.

Table 3 presents a comparison between the developed $WS_2$/AlN/Si heterostructured photodetector and previously reported $WS_2$-based photodetectors. As shown in the table, the $WS_2$/AlN/Si device exhibits a significant performance improvement compared to other $WS_2$-based photodetectors. This significant improvement is attributed to the AlN interlayer effectively suppressing leakage current and facilitating tunneling-assisted carrier transport in the SIS heterostructure [30].

## 4 Conclusion

In conclusion, $WS_2$/AlN/Si heterostructure photodetectors with systematically varied $WS_2$ thicknesses were investigated to elucidate the thickness-dependent near-infrared photoresponse at 780 nm. The combined optical and electrical analyses demonstrate that device performance is governed by a transport-limited rather than absorption-limited mechanism, with the thinnest $WS_2$ layer yielding the highest photocurrent and responsivity. Although increasing $WS_2$ thickness enhances sub-bandgap absorption and defect-related photoluminescence, the accompanying rise in trap density suppresses carrier extraction and degrades device performance under the present deposition conditions.

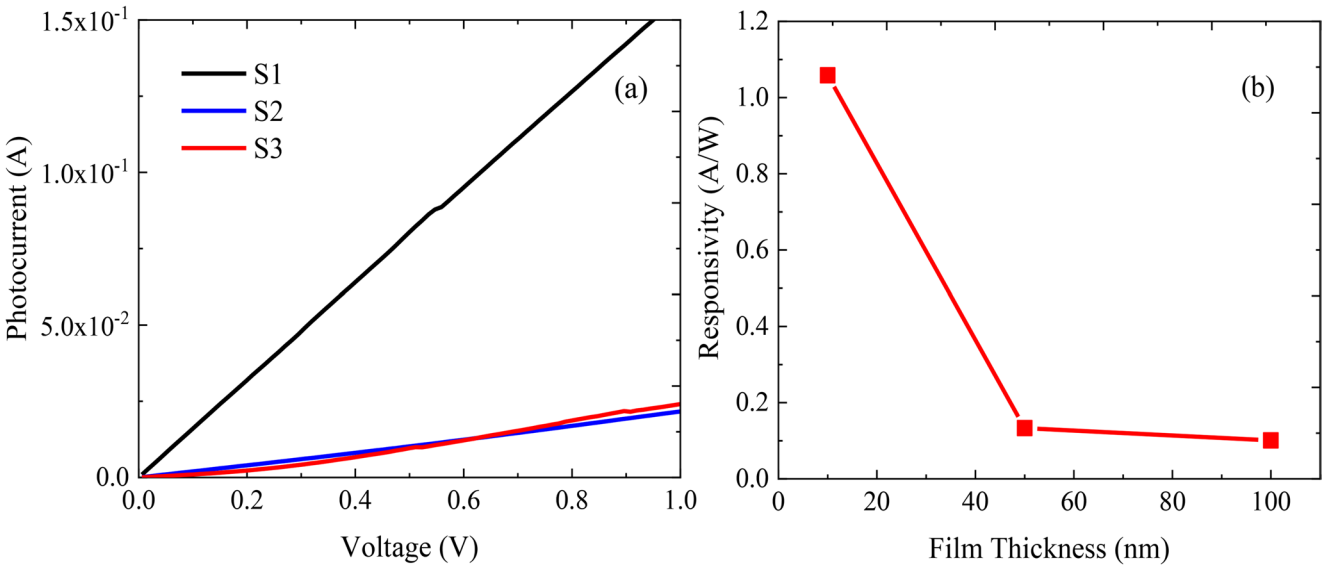



**Fig. 8** Photoresponse of fabricated $WS_2$/AlN/Si heterojunction devices: **a** photocurrent as a function of voltage, **b** responsivity as a function of $WS_2$ film thickness

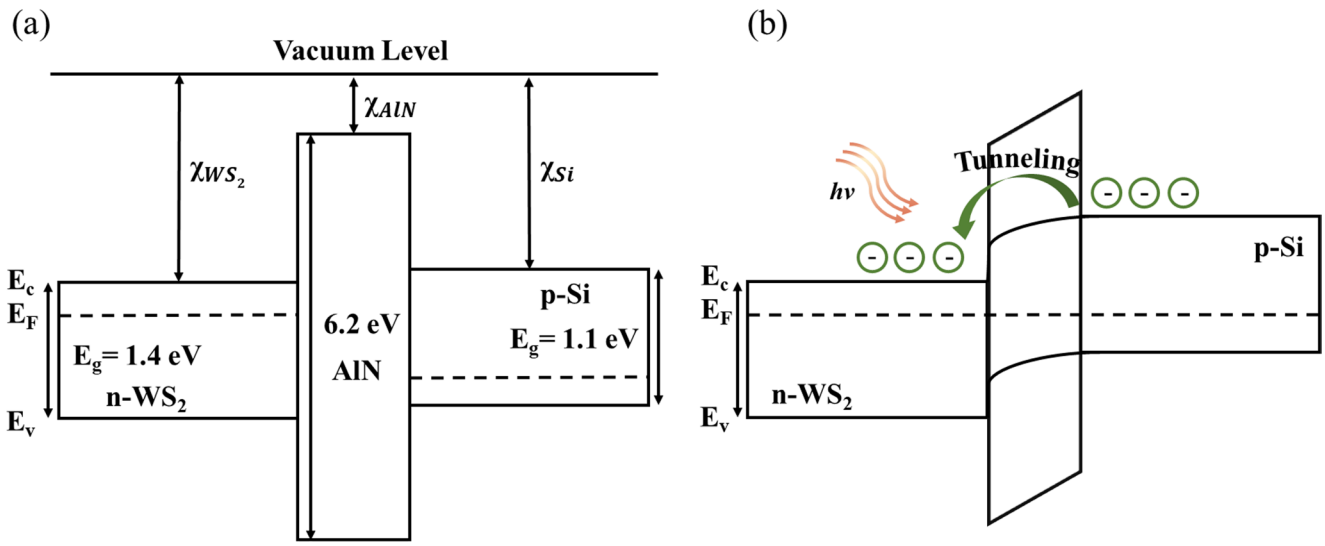



**Fig. 9** Energy band diagram and corresponding carrier transport mechanism of the $WS_2$/AlN/Si SIS heterojunction device: **a** energy band structure and (**b**) carrier transport under forward bias

**Table 3** Comparison of the characteristics of the developed $WS_2$/AlN/Si heterostructure photodetector with previously reported $WS_2$-based photodetectors

| Structure | Fabrication technique | Condition bias (V) | Responsivity (A/W) | Ref. |
|---|---|---|---|---|
| $WS_2$/Si | RF sputtering | 0 | 0.004 | [38] |
| $WS_2$/Si | CVD | 4.6 | 0.010 | [64] |
| GOQDs–$WS_2$/Si | Mechanical exfoliation | 5 | 0.012 | [65] |
| $WS_2$/Si | CVD | 5 | 0.071 | [51] |
| $WS_2$/AlN/Si | RF sputtering | 1 | 1.058 | This work |

Importantly, this behavior should not be interpreted as an intrinsic limitation of $WS_2$; rather, it reflects trap-dominated carrier dynamics associated with defect accumulation inherent to the magnetron sputtering process. Therefore, while thicker $WS_2$ layers could in principle provide enhanced absorption, their effective utilization in NIR photodetectors critically depends on defect passivation, interface engineering, and optimized growth strategies. These findings provide clear device-level design guidelines for $WS_2$/AlN-based photodetectors and highlight viable pathways toward improved performance through advanced materials and process engineering.

**Acknowledgements** The presented study was supported by Strategy and Budget Presidency (TR) with the contract 2019K12-149045.

**Authors' contributions** Dr. Donmez Kaya; Validation, Investigation, Formal analysis, Data curation, Writing – Original Draft, Visualization, Conceptualization, Methodology, Writing – Review & Editing.

**Funding** Open access funding provided by the Scientific and Technological Research Council of Türkiye (TÜBİTAK).

**Data availability** Not applicable.

## Declarations

**Conflicts of interest/Competing interests** The author declares that there are no conflicts of interest.

**Open Access** This article is licensed under a Creative Commons Attribution 4.0 International License, which permits use, sharing, adaptation, distribution and reproduction in any medium or format, as long as you give appropriate credit to the original author(s) and the source, provide a link to the Creative Commons licence, and indicate if changes were made. The images or other third party material in this article are included in the article's Creative Commons licence, unless indicated otherwise in a credit line to the material. If material is not included in the article's Creative Commons licence and your intended use is not permitted by statutory regulation or exceeds the permitted use, you will need to obtain permission directly from the copyright holder. To view a copy of this licence, visit http://creativecommons.org/licenses/by/4.0/.

## References

1. T.T. Nguyen, M. Patel, D.K. Ban, J. Kim, Vertically trigonal WS<Subscript>2</Subscript> layer embedded heterostructure for enhanced ultraviolet–visible photodetector. J. Alloys Compd. **768**, 143–149 (2018)
2. Z. Huang, T. Zhang, J. Liu, L. Zhang, Y. Jin, J. Wang, Q. Li, Amorphous $MoS_2$ photodetector with ultra-broadband response. ACS Appl. Electron. Mater. **1**, 1314–1321 (2019)
3. H.O. Dogan, F. Yıldırım, Z. Orhan, A.B. Ahmed, M. Benhaliliba, Ş Aydoğan, Numerical evaluations of curcumin organic molecule and an experimental study on hybrid photodetector performance in visible and UV regions. Org. Electron. **124**, 106946 (2024)
4. H. Qiao, Z. Huang, X. Ren, S. Liu, Y. Zhang, X. Qi, H. Zhang, Self-powered photodetectors based on 2D materials. Adv. Opt. Mater. **8**, 1900765 (2020)
5. X. Cai, Y. Luo, B. Liu, H.M. Cheng, Preparation of 2D material dispersions and their applications. Chem. Soc. Rev. **47**, 6224–6266 (2018)
6. L. Zeng, L. Tao, C. Tang, B. Zhou, H. Long, Y. Chai, Y.H. Tsang, High-responsivity UV-Vis photodetector based on transferable $WS_2$ film deposited by magnetron sputtering. Sci. Rep. **6**(1), 20343 (2016)
7. S. Ladhane, S. Shah, P. Shinde, A. Punde, A. Waghmare, Y. Hase, S.R. Jadkar, Enhanced Photoelectrochemical Activity Realized from $WS_2$ Thin Films Prepared by RF-Magnetron Sputtering for Water Splitting. ChemElectroChem **11**, e202400002 (2024)
8. S. Roy, P. Bermel, Electronic and optical properties of ultra-thin 2D tungsten disulfide for photovoltaic applications. Sol. Energy Mater. Sol. Cells **174**, 370–379 (2018)
9. A. Kumar, A. Gupta, A. Kumar, H. Surbhi, Sharma, A. Kumar, D.K. Rana, (2025). Pure $WS_2$ and nano composite $WS_2/MoS_2$ thin film based heterojunction photodetector. J. Solgel Sci. Technol., 1–13
10. N.B. Shinde, B.D. Ryu, C.H. Hong, B. Francis, S. Chandramohan, S.K. Eswaran, Growth behavior, nucleation control and excellent optical properties of atomically thin WS<Subscript>2</Subscript> thin films processed via gas-phase chemical vapor deposition. Appl. Surf. Sci. **568**, 150908 (2021)
11. S. Ito, K. Teraoka, S. Imai, N. Matsunaga, J. Jang, I. Muneta, H. Wakabayashi, *Crystallinity improvement of physical-vapor-deposited $WS_2$ films by controlling particle energy* (Japanese Journal of Applied Physics, 2024)
12. N. Akin Sönmez, Cubic MgZnO thin films on sapphire substrate: effect of deposition temperature. J. Mater. Sci. Mater. Electron. **30**(4), 4104–4110 (2019)
13. M.S. Shawkat, S.B. Hafiz, M.M. Islam, S.A. Mofid, M.M. Al Mahfuz, A. Biswas, Y. Jung, Scalable van der Waals two-dimensional PtTe2 layers integrated onto silicon for efficient near-to-mid infrared photodetection. ACS Appl. Mater. Interfaces **13**, 15542–15550 (2021)
14. C. Ling, M. Cao, X. Xue, T. Zhang, B. Feng, Q. Xue, W. Liu, Large-scale synthesis of vertically standing In2S3 nanosheets/pyramidal silicon array heterojunction for broadband photodetectors. Appl. Surf. Sci. **621**, 156901 (2023)
15. S. Chen, S. Ke, T. Ji, Z. Li, X. Xu, B. Liu, J. Zhou, High-speed self-powered PdSe2/Si 2D-3D PIN-like photodetector with broadband response based on PdSe2 quantum island structure. ACS Applied Materials & Interfaces **16**(32), 42577–42587 (2024)
16. Y. Wei, C. Lan, S. Zhou, C. Li, Recent advances in photodetectors based on two-dimensional material/Si heterojunctions. Appl. Sci. **13**(19), 11037 (2023)
17. D. Wu, Z. Lou, Y. Wang, Z. Yao, T. Xu, Z. Shi, Y.H. Tsang, Photovoltaic high-performance broadband photodetector based on MoS<Subscript>2</Subscript>/Si nanowire array heterojunction. Solar Energy Mater. Solar Cells **182**, 272–280 (2018)
18. Z. Lou, L. Zeng, Y. Wang, D. Wu, T. Xu, Z. Shi, Y.H. Tsang, High-performance MoS<Subscript>2</Subscript>/Si heterojunction broadband photodetectors from deep ultraviolet to near infrared. Opt. Lett. **42**, 3335–3338 (2017)
19. E. Wu, D. Wu, C. Jia, Y. Wang, H. Yuan, L. Zeng, X. Li, In situ fabrication of 2D WS<Subscript>2</Subscript>/Si type-II heterojunction for self-powered broadband photodetector with response up to mid-infrared. ACS Photonics **6**, 565–572 (2019)
20. S. Pal, S. Mukherjee, R. Jangir, M. Nand, D. Jana, S.K. Mandal, S.K. Ray, $WS_2$ nanosheet/Si p–n heterojunction diodes for UV–Visible broadband photodetection. ACS Appl. Nano Mater. **4**, 3241–3251 (2021)
21. S. Krishna, A.G. Reddy, N. Aggarwal, M. Kaur, S. Husale, D. Singh, G. Gupta, Enhanced current transport in GaN/AlN based single and double barrier heterostructures. Sol. Energy Mater. Sol. Cells **170**, 160–166 (2017)
22. A.M. Chowdhury, G. Chandan, R. Pant, B. Roul, D.K. Singh, K.K. Nanda, S.B. Krupanidhi, Self-powered, broad band, and ultrafast InGaN-based photodetector. ACS Appl. Mater. Interfaces. **11**(10), 10418–10425 (2019)
23. N.A.K. Jadoon, V. Puvanenthiram, M.A.H. Mosa, A. Sharma, K. Wang, Recent advances in aluminum nitride (AlN) growth by magnetron sputtering techniques and its applications. Inorganics **12**(10), 264 (2024)
24. D.K. Singh, R. Pant, A.M. Chowdhury, B. Roul, K.K. Nanda, S.B. Krupanidhi, Defect-mediated transport in self-powered, broadband, and ultrafast photoresponse of a $MoS_2$/AlN/Si-based photodetector. ACS Appl. Electron. Mater. **2**(4), 944–953 (2020)

25. K. Kumar, R. Yadav, S. Husale, P. Singh, D. Kaur, Ultrafast photoresponse in n-$MoS_2$/AlN/p-Si (SIS) heterojunction based visible to NIR photodetectors. Sol. Energy Mater. Sol. Cells **246**, 111942 (2022)
26. S.Y. Wang, S.J. Chang, Y.C. Huang, J.H. Chih, Y.C. Lin, C.C. Cheng, C.H. Chien, (2023). Conformal bilayer h-AlN epitaxy on $WS_2$ by ALD with ultralow leakage current. Appl. Phys. Lett., **123**(16)
27. M. Akhtaruzzaman, M. Shahiduzzaman, N. Amin, G. Muhammad, M.A. Islam, K.S.B. Rafiq, K. Sopian, Impact of ar flow rates on micro-structural properties of $WS_2$ thin film by RF magnetron sputtering. Nanomaterials **11**(7), 1635 (2021)
28. Q. Zhao, J. Xu, X.Y. Xu, Z. Wang, D.P. Yu, Field emission from AlN nanoneedle arrays. Appl. Phys. Lett. **85**(22), 5331–5333 (2004)
29. I. Hotovy, L. Spiess, M. Mikolasek, I. Kostic, M. Sojkova, H. Romanus, V. Rehacek, Layered $WS_2$ thin films prepared by sulfurization of sputtered W films. Appl. Surf. Sci. **544**, 148719 (2021)
30. M. Benhaliliba, M.D. Kaya, S. Özçelik, C.E. Benouis, K. Dris, Fabrication and characterization of $WS_2$/AlN/Si SIS heterojunction for emergent material photovoltaic applications. Appl. Phys. A **131**(4), 269 (2025)
31. P. Sumathi, J. Chandrasekaran, R. Marnadu, S. Muthukrishnan, S. Maruthamuthu, Synthesis and characterization of tungsten disulfide thin films by spray pyrolysis technique for n-$WS_2$/p-Si junction diode application. J. Mater. Sci. Mater. Electron. **29**(19), 16815–16823 (2018)
32. Y. Zhang, S. Feng, J. Guo, R. Tao, Z. Liu, X. He, Y. Wang, $WS_2$ with controllable layer number grown directly on W film. Nanomaterials **14**(16), 1356 (2024)
33. S.Y. Cho, Y.H. Kang, J.Y. Jung, S.Y. Nam, J. Lim, S.C. Yoon, C. Lee, Novel zinc oxide inks with zinc oxide nanoparticles for low-temperature, solution-processed thin-film transistors. Chem. Mater. **24**(18), 3517–3524 (2012)
34. B.H. Kim, H. Yoon, S.H. Kwon, D.W. Kim, Y.J. Yoon, Direct $WS_2$ photodetector fabrication on a flexible substrate. Vacuum **184**, 109950 (2021)
35. M. Benhaliliba, A. Ayeshamariam, Y.S. Ocak, The nanostructure based SnS chalcogenide semiconductor: a detailed investigation of physical and electrical properties. Period. Polytech. Chem. Eng. **68**(3), 326–337 (2024)
36. G.Q. Jiang, C.B. Yao, S.B. Bao, Y. Cai, Standing growth mechanism and ultrafast nonlinear absorption properties of WS2 films. Opt. Mater. **106**, 109995 (2020)
37. H.S. Kim, M. Patel, J. Kim, M.S. Jeong, Growth of wafer-scale standing layers of WS<Subscript>2</Subscript> for self-biased high-speed UV–visible–NIR optoelectronic devices. ACS Appl. Mater. Interfaces **10**(4), 3964–3974 (2018)
38. Y.P. Goswami, P.K. Gupta, A. Pandey, Hydrothermally synthesized $WS_2$-QDs/Si (0-D/3-D) vertical heterojunction for an efficient wide spectral (UV–Vis–NIR) photodetection. IEEE Trans. Electron. Devices. **71**(5), 3084–3089 (2024)
39. M.J. Park, K. Park, H. Ko, Near-infrared photodetector achieved by chemically-exfoliated multilayered MoS<Subscript>2</Subscript> flakes. Appl. Surf. Sci. **448**, 64–70 (2018)
40. A. Splendiani, L. Sun, Y. Zhang, T. Li, J. Kim, C.Y. Chim, F. Wang, Emerging photoluminescence in monolayer MoS2. Nano Lett. **10**(4), 1271–1275 (2010)
41. W. Zhao, Z. Ghorannevis, L. Chu, M. Toh, C. Kloc, P.H. Tan, G. Eda, Evolution of electronic structure in atomically thin sheets of WS2 and WSe2. ACS Nano. **7**(1), 791–797 (2013)
42. K.F. Mak, C. Lee, J. Hone, J. Shan, T.F. Heinz, Atomically thin MoS 2: a new direct-gap semiconductor. Phys. Rev. Lett. **105**(13), 136805 (2010)
43. S. Tongay, J. Zhou, C. Ataca, J. Liu, J.S. Kang, T.S. Matthews, J. Wu, Broad-range modulation of light emission in two-dimensional semiconductors by molecular physisorption gating. Nano Lett. **13**(6), 2831–2836 (2013)
44. M.A. Reshchikov, H. Morkoç, (2005). Luminescence properties of defects in GaN. J. Appl. Phys., **97**(6)
45. B.C. Johnson, B. Haberl, J.E. Bradby, J.C. McCallum, J.S. Williams, Temperature dependence of Raman scattering from the high-pressure phases of Si induced by indentation. Phys. Rev. B **83**(23), 235205 (2011)
46. O. Lopez-Sanchez, D. Lembke, M. Kayci, A. Radenovic, A. Kis, Ultrasensitive photodetectors based on monolayer MoS2. Nature nanotechnology **8**(7), 497–501 (2013)
47. E.C. Tyo, S. Vajda, Catalysis by clusters with precise numbers of atoms. Nat. Nanotechnol. **10**(7), 577–588 (2015)
48. C. Ruppert, A. Chernikov, H.M. Hill, A.F. Rigosi, T.F. Heinz, The role of electronic and phononic excitation in the optical response of monolayer WS2 after ultrafast excitation. Nano Letters **17**(2), 644–651 (2017)
49. F. Bai, J. Qi, F. Li, Y. Fang, W. Han, H. Wu, Y. Zhang, A high-performance self-powered photodetector based on monolayer MoS<Subscript>2</Subscript>/perovskite heterostructures. Adv. Mater. Interfaces **5**(6), 1701275 (2018)
50. M. Benhaliliba, A. Ben Ahmed, Innovative device based brilliant green dye material for optoelectronic and nonlinear optic applications. Chemistry Africa **7**(3), 1629–1638 (2024)
51. M. Benhaliliba, Y.S. Ocak, The inventive manufacturing and characterization of Au/BG/p-Si/Al devices for solar cell applications. Appl. Phys. A **130**(6), 371 (2024)
52. Z. Yue, H. Shen, C. Wang, Y. Xu, Y. Li, J. Zheng, L. Wang, Ultrafast and self-driven flexible photodetector based on vertical $MoS_2$/Si heterojunction through enhanced light-trapping structures and $Al_2O_3$ interface passivation. Appl. Surf. Sci. **655**, 159630 (2024)
53. M. Shahbazi, R. Mohammadkhani, High performance in the DC sputtering-fabricated Au/WS<Subscript>2</Subscript> optoelectronic device. Sci. Rep. **15**(1), 12721 (2025)
54. B. He, Z.Q. Ma, J. Xu, L. Zhao, N.S. Zhang, F. Li, Y.T. Yin, Realization and characterization of an ITO/AZO/$SiO_2$/p-Si SIS heterojunction. Superlattices Microstruct. **46**(4), 664–671 (2009)
55. F. Yildirim, M. Taşkin, A. Ahmed, M. Benhaliliba, Ü. İncekara, Ş. Aydoğan, (2025). Enhanced photoresponse in MIS-type UV-Vis photodetector via biocompatible glutathione (C10H17N3O6S) interlayer: theoretical and experimental analysis. Emergent Mater., **8**(7)
56. J. Yin, L. Liu, Y. Zang, A. Ying, W. Hui, S. Jiang, J. Kang, *Engineered tunneling layer with enhanced impact ionization for detection improvement in graphene/silicon heterojunction photodetectors*, vol. 10 (Science & Applications, Light, 2021), p.113
57. M.M.S. Villamayor, A. Lindblad, F.O. Johansson, T. Tran, N.H. Pham, D. Primetzhofer, F.O.L. Johansson, N.L.A.N. Sorgenfrei, E. Giangrisotomi, A. Föhlisch, P. Lourenço, R. Bernard, N. Witkowski, G. Prévot, T. Nyberg, Growth of two-dimensional WS<Subscript>2</Subscript> thin films by reactive sputtering. Vacuum **188**, 110205 (2021)
58. Z.D. Sha, X.M. Wu, L.J. Zhuge, The structure and optical properties of SiC film on Si (111) substrate with a ZnO buffer layer by RF-magnetron sputtering technique. Phys. Lett. A **355**(3), 228–232 (2006)
59. A.M. Alsaad, Q.M. Al-Bataineh, I.A. Qattan, A.A. Ahmad, A. Ababneh, Z. Albataineh, A. Telfah, Measurement and ab initio investigation of structural, electronic, optical, and mechanical properties of sputtered aluminum nitride thin films. Front. Phys. **8**, 115 (2020)
60. M. Patel, P.M. Pataniya, V. Patel, C.K. Sumesh, D.J. Late, Large area, broadband and highly sensitive photodetector based on ZnO-WS<Subscript>2</Subscript>/Si heterojunction. Solar Energy **206**, 974–982 (2020)

61. S. Kaushik, T.R. Naik, A. Alka, M. Garg, B.R. Tak, M. Ravikanth, R. Singh, Surface modification of AlN using organic molecular layer for improved deep UV photodetector performance. ACS Appl. Electron. Mater. **2**(3), 739–746 (2020)
62. B. Hussain, A. Aslam, T.M. Khan, M. Creighton, B. Zohuri, Electron affinity and bandgap optimization of zinc oxide for improved performance of ZnO/Si heterojunction solar cell using PC1D simulations. Electronics. **8**(2), 238 (2019)
63. Y.R. Nik et al., High-performance $CsGeBr_3$ perovskite/$WS_2$ Nano-Flakes Field-Effect transistor at high temperature. Opt. Mater. **132**, 112757 (2022)
64. H.J.W. Li, K. Huang, Y. Zhang, Enhanced photoresponsivity of the GOQDs decorated WS<Subscript>2</Subscript> photodetector. Mater. Res. Express **6**, 045902 (2019)
65. A. Roy, P. Kalita, B. Mondal, Structural, spectroscopic and electrical properties of liquid phase exfoliated few layered two-dimensional tungsten disulfide ($WS_2$ ) using anionic surfactant. J. Mater. Sci. Mater. Electron. **34**, 224 (2023)

**Publisher's note** Springer Nature remains neutral with regard to jurisdictional claims in published maps and institutional affiliations.